Reflector-Based 3D Tomographic Ultrasound Reconstruction: Simulation Study

Bhaskara R. Chintada[1], Sergio J. Sanabria[1], Wolfgang Bost[2], Orcun Goksel[1]

[1] *Computer-assisted Applications in Medicine, Dept. of Information Tech. and Electrical Eng., ETH Zurich, Switzerland*
[2] *Fraunhofer Institute for Biomedical Engineering, Sankt Ingbert, Germany*

Abstract—**Ultrasound Computer Tomography (USCT) is used to map local wave propagation parameters, such as speed-of-sound (SoS), as potential imaging biomarkers. Reflector-based USCT is a technique for the implementation of USCT using commercial transducer arrays, in contrast to complex USCT hardware setups requiring suspension in a water bath. In this work, we model a prototype 2D-matrix transducer and study reflector-based 3D-USCT reconstruction feasibility and resolution via numerical simulations. Modeling the ultrasound wavefronts using rays, we employ 3D-ray tracing methods to compute acoustic travel paths on a reconstruction voxel grid, and subsequently utilize optimization techniques to solve the inverse problem of SoS reconstruction. We show the feasibility of generating 3D USCT images and study the resolution for varying tissue SoS contrast.**

Index Terms—**Imaging speed-of-sound, ultrasound computed tomography, ray tracing**

I. INTRODUCTION

Ultrasound Computed Tomography (USCT) is a medical imaging technique, which can complement the conventional ultrasound B-mode imaging that is cost-effective, real-time and non-ionizing. USCT images the local ultrasound wave propagation parameters such as speed-of-sound (SoS), attenuation, and refractive indices, since these parameters may facilitate differentiation of different tissue compositions and thereby potentially helping in diagnosis [1]–[4]. Current proposed USCT systems are based on submerging the target anatomical structure in a water bath, which is equipped with a large number of cylindrically/spherically positioned transducer elements at known locations [5], [6]. Such transmission USCT systems have great potential for *in-vivo* breast cancer screening. In these setups, the transducer elements are operated in multi-static mode, i.e., after the emission of a wave by a single element of the transducer array, all peripherally arranged transducer elements simultaneously receive the RF signals. This procedure is repeated for each transducer element. Based on such multi-static data acquisition, the time-of-flight (ToF) for transducer-receiver combination can be computed by detecting the first arrival of the wavefront. Such ToF measurements, as well as their amplitudes and other parameters, allow the reconstruction of SoS and attenuation maps, similarly to X-ray computed tomography (CT).

Naturally it is beneficial to develop SoS and attenuation imaging to be compatible with existing conventional ultra-sound transducers in order to avail several logistic advantages of commercial transducer arrays, also for SoS imaging in the clinics. This was also the target of several earlier studies in the literature. Robinson et al. [7] proposed a method for determining speed of ultrasound propagation in tissue by using ray-tracing and analyzing the pulse-echo data obtained from a compound scan. It works based on the following: If the imaged region does not have the presumed uniform speed, this would then result in mis-registration of point sources, leading to a blurred B-mode image. Similarly, Hayashi et al. [8] proposed a method for measuring in-vivo SoS in the reflection mode by dynamically correcting delays in receive beam forming until the operator observes a known anatomical structure without any blur. This technique was used in measuring the SoS in liver while using the diaphragm as a reference structure to observe, until the operator judged it to have the least blur. In order to automatize this approach, Shin et al. [9] developed an iterative method using blind convolution to estimate SoS. Ophir and Caspedes [10], [11] introduced an alternative method by positioning coplanar single element transducers such that their beams intersected in the vicinity of the target medium; from this intersection of beams, an initial ToF is computed and one at a time these transducer elements shifted by known distances. The average SoS was calculated from a least square fit to time vs. known position shifts plot. This method was later implemented using a conventional linear array ultrasound transducer [12]. Ophir et al. [13] developed another method to estimate speed-of-sound by compressing the soft tissue with a transducer to a known depth and comparing the temporal changes between pre- and post-compression pulse-echo sequences. Indeed, many such development also marked the beginning of *elastography*, which aims to measure local strains by imaging compressed tissue.

In the techniques above, the goal was to extract a homogeneous-equivalent (average) SoS in the region, or part thereof; often aiming to utilize this in beamforming for sharper B-mode images. In contrast, Krueger et al. [14] proposed to reconstruct a SoS map of the tissue by positioning an acoustic reflector at a known depth as a timing reference for calculating ToF values robustly when the transducer is operated in multi-static mode. It was initially proposed to be used as an add-on to the X-ray mammography compression plate. Despite following studies in this direction [15], error-prone reflector delineation and tomographic reconstruction methods have long hindered accurate and high-resolution SoS imaging with a
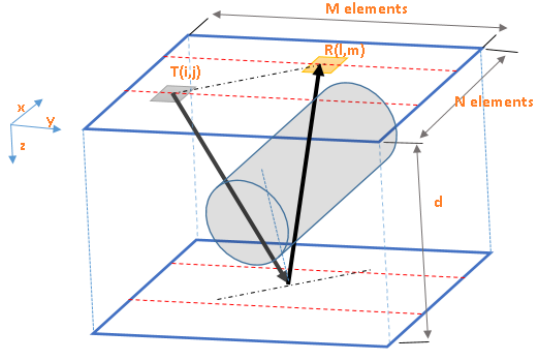
Fig. 1. A 2D-matrix array with an acoustic reflector placed at a distance d. Wavefront arrival is modeled using rays, where each ray path originates from a transmitting Tx element T(i,j), bouncing from the reflector, and arriving at a receiving Rx element R(l,m), where $i,l \in \{1..N\}$ and $j,m \in \{1..M\}$.

reflector. Recently, Sanabria et al. [16] reported reflector-based SoS imaging using dynamic-programing based reflector delineation and angular-weighted total-variation regularization techniques. Thanks to this combination of techniques, they achieved sharp inclusion delineation, without a need of prior inclusion segmentation. This method has high accuracy and resolution compared to earlier reflector-based techniques in the literature. There is a growing interest and demand for volumetric ultrasound imaging (3D/4D). We aim to extend the above 2D reflector-based technique [16] to 2D matrix transducers for 3D SoS imaging. Feasibility of 3D reflector-based SoS reconstruction is studied in this paper using numerical phantom simulations.

II. METHODS

A. Forward problem of sound propagation

A 2D-matrix transducer with NxM elements is operated in multi-static mode. An acoustic reflector is positioned at a distance of d from the transducer as in Fig.1. For acoustic propagation, refractions are ignored and the travel of the acoustic wave from transmitting to receiving element is modeled using a straight ray. Time-of-flight, t_i, of each acoustic ray i then relates to the *slowness s* (inverse of speed) along the traversed ray path as follows:

$$t_i = \int_{p_i} s \, dl \qquad (1)$$

where p_i represents the acoustic ray path and l is the traversed distance. For a non-refracting acoustic path, the first wavefront from an transducer element transmission Tx reflected from the reflector arrives at any receiving element Rx following the (shortest) path being reflected at the mid-point of the line segment between Tx and Rx element locations projected on the reflector.

To cast this as a tomographic reconstruction problem, the relation above can be discretized on a Cartesian 3D voxel grid as

$$t_i = \sum_{n=1}^{N_i} s_k l_{ik} \qquad (2)$$

where s_k represents the slowness in the k'th voxel along the i ray of N_i voxels, and l_{ik} represents the partial acoustic path length of ray i within this k'th voxel. Collocating Eq.2 for each ray path along all Tx-Rx combinations, the forward-problem of sound propagation can then be represented with the following system of linear equations

$$\mathbf{Ls} = \mathbf{t} \qquad (3)$$

where $\mathbf{t}$ is the column vector of ToF values along all ray paths, $\mathbf{s}$ is the column vector of slowness values for all grid voxels, and the system matrix $\mathbf{L}$ encodes the discretized ray integrals for each ray onto the voxel grid. Note that $\mathbf{L}$ is constant for given transducer geometry and reflector position.

B. Inverse problem of SoS reconstruction

Given ToF measurements, one can then solve an inverse problem to reconstruct local slowness, and thereby an SoS image. If the number of ToF measurements (Tx-Rx combinations) are much higher than the number of voxels in the reconstruction grid, then an optimal solution may be calculated using least squares, as follows

$$\hat{\mathbf{s}} = \arg\min_{\mathbf{s}} ||\mathbf{Ls} - \mathbf{t}||_2 \ . \qquad (4)$$

However, in most practical scenarios based on the Tx-Rx pairs and the definition of the reconstruction grid, this problem easily becomes ill-posed, with reconstructions highly susceptible to noise in the ToF measurements. System conditioning is affected by the acoustic rays only traveling through a small number of voxels for each measurement. Additional source of errors negatively affecting robustness include: (1) Straight acoustic path assumptions may fail due to refractions and SoS inhomogeneities; (2) assumed reflector depth/orientation may be incorrect; and most importantly, (3) ToF measurements by the reflector delineation algorithm may contain small inaccuracies as well as grossly-incorrect outliers. To ensure robustness, we enforce spatial regularization as follows:

$$\hat{\mathbf{s}} = \arg\min_{\mathbf{s}} ||\mathbf{Ls} - \mathbf{t}||_2 + \lambda ||\mathbf{Ds}||_{\mathbf{n}} \qquad (5)$$

where $\mathbf{D}$ is the difference operator encoding discrete derivatives in all three axes, n is the regularization norm, and λ is the regularization weighting. $n=2$ is the well-known Tikhonov Regularization (TR) that quadratically penalizes differences between neighboring voxels. Favors smaller gradients, this prevents sharp edges between different image regions, producing smooth (blurred) images. In contrast, with $n=1$ known as the Total Variation Regularization (TVR), sharp and smooth gradients are equally weighted, helping in preserving edges.

The ray-tracing algorithm for populating the sparse system matrix $\mathbf{L}$ was implemented in Matlab. Ray projections within each traversed voxel were computed using a ray-box intersection algorithm [17].
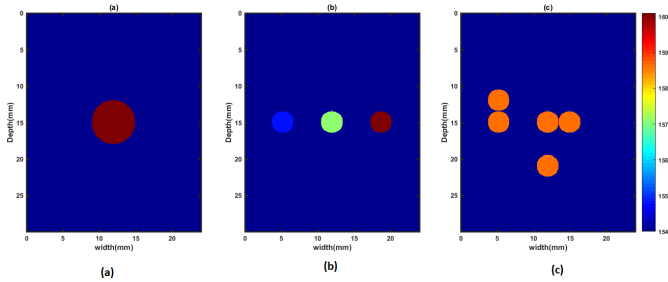
Fig. 2. Cross-sections of numerical phantoms used for testing the proposed reconstruction method. Given 1540 m/s background, (a) the feasibility phantom (FP) with a ⌀6 mm cylindrical inclusion of 4% SoS contrast, (b) a contrast phantom (CP) with ⌀3 mm inclusions of 0.5%, 2%, and 4% SoS contrasts, and (c) resolution phantom (RP) with 3% SoS contrast inclusions placed horizontally and vertically next to each other.

III. NUMERICAL EXPERIMENTS

We modeled a 2D-matrix transducer with 32x16 elements of 0.75 mm pitch in both directions. The acoustic reflector is considered to be positioned at 30 mm depth from and in parallel to the transducer surface. For different numerical phantoms, we simulated ToF values using the forward problem in Eq.(3), by assuming straight sound paths. Then, for different numerical phantoms and simulated noise studies, SoS images were reconstructed by solving the inverse problem using optimization methods in the CVX package [18]

Figure 2 illustrates the numerical phantoms that we used in this work. To demonstrate the feasibility of 3D SoS imaging, we generated a feasibility phantom (FP) with a ⌀6 mm cylindrical and spherical inclusions of 4% SoS contrast with respect to a background SoS value of 1540 m/s. This is reasonable range of SoS contrast because diseased soft tissue's sound of speed ranges withing 5% of this background value, with pathologies being often stiffer. Next, in order to study the contrast capability, we used a numerical contrast phantom (CP) consisting of ⌀3 mm cylindrical inclusions of 0.5%, 2% and 4% SoS contrast. To evaluate resolution, we generated a resolution phantom (RP) with nearby as well as farther away inclusions, both axially and laterally, as seen in Fig. 2(c).

IV. RESULTS AND DISCUSSION

Figure 3 illustrates a rendering of the reconstructed volume and cross-sectional image slices from the single cylindrical inclusion feasibility phantom FP, using Tikhonov and TVR regularizations. For volume renderings in all reconstruction figures, a linear alpha (transparency) map is used corresponding to the color-bar range of values from 1540 to 1601. The reconstructed images have mean(±std) SoS values of 1600.4(±3.3) m/s and 1540(±0.5) m/s, respectively, for the inclusion and background regions by using TVR; in comparison to 1584.3(±6.2) m/s and 1540.6(±4.8) m/s for using TR. By comparing (b) & (d) it is seen that TVR helps in maintaining the sharp boundaries in the reconstructed volume.

Figure 4 illustrates a rendering of the reconstructed volume and cross-sectional image slices from the single spherical
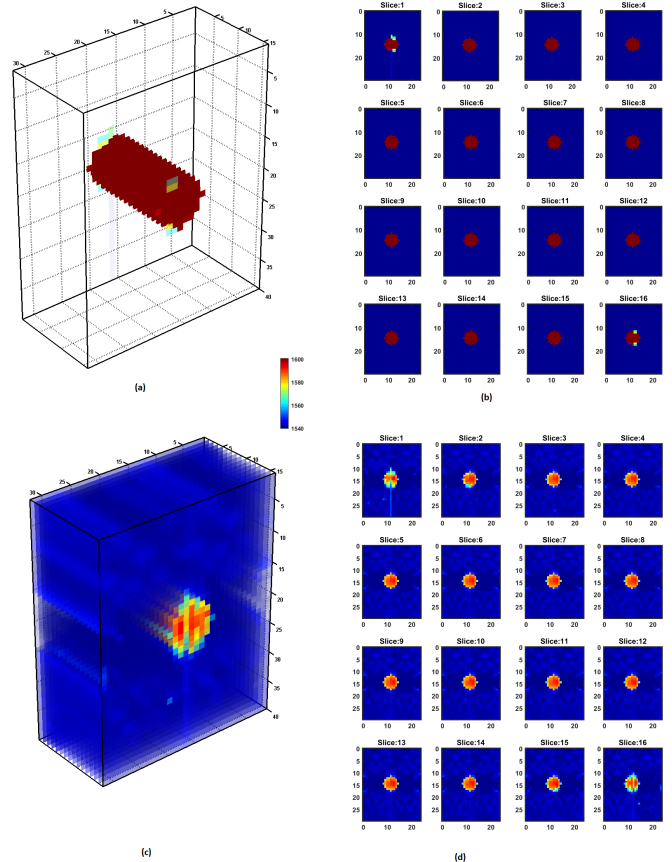

Fig. 3. 3D volume renderings (left) and cross-sectional images (right) from reconstructed volumes of single-inclusion feasibility phantom FP, using TVR (upper row) and TR (lower row).

inclusion feasibility phantom FP, using TVR regularizations. SoS values of 1601(±0.004) m/s and 1540(±0.00049) m/s were reconstructed, respectively, for the inclusion and background regions by using TVR. In these ideal conditions, the reconstruction is seen to be very accurate.

Figure 5 shows the reconstructed images of CP. It can be seen that even the lowest 0.5% SoS contrast was reconstructed faithfully. SoS values were found to be 1547.4(±1.1) m/s, 1568.5(±5.5) m/s and 1600.1(±5.8) m/s, respectively, in the 0.5%, 2% and 4% SoS inclusions, with 1540.1(±0.8) m/s in the background.

Figure 6 shows the reconstructed SoS images for RP. It can be seen that both horizontal and vertical inclusions are separable, except for the two end-slices where there are not sufficient number of overlapping observations.

V. CONCLUSIONS

In this simulation study, we have presented a formalized framework for reflector-based 3D reconstruction of local speed-of-sound using 3D ray-tracing methods to compute acoustic ray projections on a voxel grid. Under ideal conditions with no acoustic refractions and no noise in time-of-flight estimations, both contrast and resolution of reconstructions were shown to be relatively good.
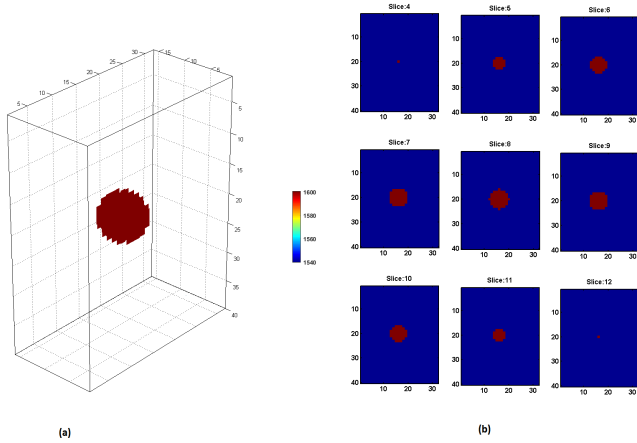
Fig. 4. 3D volume renderings (left) and cross-sectional images (right) from reconstructed volumes of single-inclusion spherical feasibility phantom (FP), using TVR.
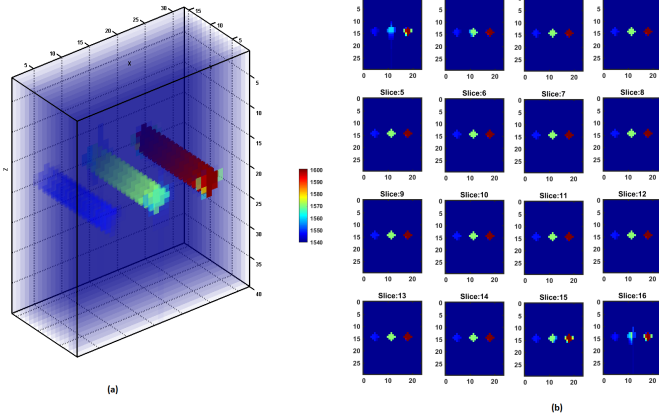

Fig. 5. 3D volume rendering (left) and cross-sectional images (right) from the reconstructed volumes of the contrast phantom CP using TVR.
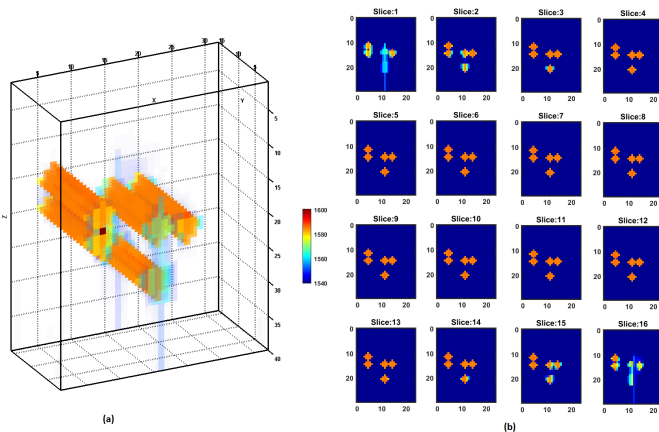

Fig. 6. 3D volume rendering (left) and cross-sectional images (right) from the reconstructed volumes of the contrast phantom CP using TVR.

REFERENCES

[1] J. Bamber and C. Hill, "Acoustic properties of normal and cancerous human liveri. dependence on pathological condition," *Ultrasound in medicine & biology*, vol. 7, no. 2, pp. 121–133, 1981.

[2] N. Duric, P. Littrup, L. Poulo, A. Babkin, R. Pevzner, E. Holsapple, O. Rama, and C. Glide, "Detection of breast cancer with ultrasound tomography: First results with the computed ultrasound risk evaluation (cure) prototype," *Medical physics*, vol. 34, no. 2, pp. 773–785, 2007.

[3] N. Duric, P. Littrup, O. Rama, and E. Holsapple, "Computerized ultrasound risk evaluation (cure): first clinical results," *Acoustical Imaging*, pp. 173–181, 2007.

[4] J.-W. Jeong, D. C. Shin, S.-H. Do, C. Blanco, N. E. Klipfel, D. R. Holmes, L. J. Hovanessian-Larsen, and V. Z. Marmarelis, "Differentiation of cancerous lesions in excised human breast specimens using multiband attenuation profiles from ultrasonic transmission tomography," *Journal of Ultrasound in Medicine*, vol. 27, no. 3, pp. 435–451, 2008.

[5] J. F. Greenleaf and R. C. Bahn, "Clinical imaging with transmissive ultrasonic computerized tomography," *IEEE Transactions on Biomedical Engineering*, no. 2, pp. 177–185, 1981.

[6] H. Gemmeke and N. Ruiter, "3d ultrasound computer tomography for medical imaging," *Nuclear Instruments and Methods in Physics Research Section A: Accelerators, Spectrometers, Detectors and Associated Equipment*, vol. 580, no. 2, pp. 1057–1065, 2007.

[7] D. Robinson, F. Chen, and L. Wilson, "Measurement of velocity of propagation from ultrasonic pulse-echo data," *Ultrasound in medicine & biology*, vol. 8, no. 4, pp. 413 417–415 420, 1982.

[8] N. Hayashi, N. Tamaki, M. Senda, K. Yamamoto, Y. Yonekura, K. Torizuka, T. Ogawa, K. Katakura, C. Umemura, and M. Kodama, "A new method of measuring in vivo sound speed in the reflection mode," *Journal of clinical ultrasound*, vol. 16, no. 2, pp. 87–93, 1988.

[9] H.-C. Shin, R. Prager, H. Gomersall, N. Kingsbury, G. Treece, and A. Gee, "Estimation of average speed of sound using deconvolution of medical ultrasound data," *Ultrasound in medicine & biology*, vol. 36, no. 4, pp. 623–636, 2010.

[10] J. Ophir, "Estimation of the speed of ultrasound propagation in biological tissues: A beam-tracking method," *IEEE transactions on ultrasonics, ferroelectrics, and frequency control*, vol. 33, no. 4, pp. 359–368, 1986.

[11] I. Céspedes, J. Ophir, and Y. Huang, "On the feasibility of pulse-echo speed of sound estimation in small regions: Simulation studies," *Ultrasound in medicine & biology*, vol. 18, no. 3, pp. 283–291, 1992.

[12] M. Kondo, K. Takamizawa, M. Hirama, K. Okazaki, K. Iinuma, and Y. Takehara, "An evaluation of an in vivo local sound speed estimation technique by the crossed beam method," *Ultrasound in medicine & biology*, vol. 16, no. 1, pp. 65–72, 1990.

[13] J. Ophir and Y. Yazdi, "A transaxial compression technique (tact) for localized pulse-echo estimation of sound speed in biological tissues," *Ultrasonic Imaging*, vol. 12, no. 1, pp. 35–46, 1990.

[14] M. Krueger, V. Burow, K. Hiltawsky, and H. Ermert, "Limited angle ultrasonic transmission tomography of the compressed female breast," in *Ultrasonics Symposium, 1998. Proceedings., 1998 IEEE*, vol. 2. IEEE, 1998, pp. 1345–1348.

[15] S.-W. Huang and P.-C. Li, "Computed tomography sound velocity reconstruction using incomplete data," *IEEE transactions on ultrasonics, ferroelectrics, and frequency control*, vol. 51, no. 3, pp. 329–342, 2004.

[16] S. J. Sanabria and O. Goksel, "Hand-held sound-speed imaging based on ultrasound reflector delineation," in *International Conference on Medical Image Computing and Computer-Assisted Intervention*. Springer, 2016, pp. 568–576.

[17] A. Williams, S. Barrus, R. K. Morley, and P. Shirley, "An efficient and robust ray-box intersection algorithm," in *ACM SIGGRAPH 2005 Courses*. ACM, 2005, p. 9.

[18] M. Grant and S. Boyd, "CVX: Matlab software for disciplined convex programming, v2.0," http://cvxr.com/cvx.